Effect of Erroneous Position Measurements in Vector-Controlled Doubly Fed Induction Generator

Zhong Wang, *Student Member, IEEE*, Guo-Jie Li, Yuanzhang Sun, *Senior Member, IEEE*, and Boon Teck Ooi, *Life Fellow, IEEE*

***Abstract*—Vector control of the doubly fed induction generators (DFIGs) depends on accurate information from a stator voltage phase lock loop (PLL) and a rotor position encoder for the reference frame transformations required by theory. The effect of erroneous information due to noise picked up by commonly used hardware PLLs and incremental position encoders was analyzed in this paper. The analysis shows that erroneous information can give rise to destructively large currents due to: 1) the DFIG system wrongfully perceiving very large *P* and *Q* references; and 2) system instability. It is shown that instability does not arise from inside the inner current feedback loop, but from the outer feedback loop that regulates the complex power. Simulation and experimental test results validate the analysis. The experimental results are taken from a 1.5-MW DFIG intended for a wind turbine. A simple scheme to protect against the erroneous information has been tested successfully in a brief trial period.**

***Index Terms*—Angular measurement, disturbance, doubly fed induction generator (DFIG), stability, vector control, wind power.**

NOMENCLATURE

$u_{ds}, u_{qs}, u_{dr}, u_{qr}$	Two-axis voltages.
$i_{ds}, i_{qs}, i_{dr}, i_{qr}$	Two-axis currents.
$\psi_{ds}, \psi_{qs}, \psi_{dr}, \psi_{qr}$	Two-axis flux linkages.
L_s, L_r	Machine inductances.
L_m	Mutual inductances.
r_s, r_r	Machine resistances.
ω_s, ω_r	Stator and slip angular frequency.
ω_m	Rotor angular frequency.
θ_s, θ_r	Stator and rotor angle.
θ_{sr}	Slip angle.
P_s, Q_s	Stator active and reactive power.
σ	Leakage factor.
J	Moment of inertia.
T_{em}	Electromagnetic torque.
T_m	Input torque.
s	Rotor slip.
p	Differential operator.
Superscripts	
$*$	Reference value.
p	Power loop parameters.
c	Current loop parameters.
$\wedge$	Observed value.
Subscripts	
d, q	d–q (synchronous) axes.
s, r	Stator, rotor.

Manuscript received July 17, 2009; revised October 7, 2009. First published January 29, 2010; current version published February 17, 2010. This work was supported in part by BP Alternative Energy and by the National Natural Science Foundation of China under Grant 50823001 and Grant 50977050. Paper no. TEC-00284-2009.

Z. Wang, G.-J. Li, and Y. Sun are with the Department of Electrical Engineering, Tsinghua University, Beijing 100084, China (e-mail: wangzhong06@mails.tsinghua.edu.cn; liguojie@mail.tsinghua.edu.cn; yzsun@mail.tsinghua.edu.cn).

B. T. Ooi is with the Department of Electric and Computer Engineering, McGill University, Montreal, QC H3 A 2A7, Canada (e-mail: boon-teck.ooi@mcgill.ca).

Color versions of one or more of the figures in this paper are available online at http://ieeexplore.ieee.

Digital Object Identifier 10.1109/TEC.2009.2037216

I. INTRODUCTION

DOUBLY fed induction generator (DFIG) technology is widely adopted in wind turbine application because the rotor-side back-to-back converters, which control active and reactive powers independently, are rated at the maximum slip (around 0.3), and are therefore cheaper. Fig. 1 shows typical connection of a DFIG-based wind turbine system to an infinite-bus power system [1].

One task of the grid-side converter shown in Fig. 1 is to convey the slip power from the rotor to the grid. This is achieved automatically by keeping the dc-link voltage constant. Its secondary role is to provide reactive power to assist in voltage support. The main control strategy of the DFIG is implemented on the rotor-side converter to regulate the active and reactive powers. Among all the control schemes, the vector control is the most popular [2]–[4]. Decoupled control of active and reactive powers is accomplished by aligning the *d*-axis either to the stator flux linkage [2], [3] or the stator voltage [4].

Vector control depends on the transformation of voltages and currents from the *a*–*b*–*c* reference frame to the *d*–*q* reference frame. Critical information in the transformations are: 1) position of the rotor winding axes with respect to the stator winding axes and 2) the stator voltage angle. The rotor position is obtained by a position encoder (incremental or absolute). The stator angle is obtained by hardware or software phase lock loop (PLL).

The criticality of the angular measurements has been made clear from insulated gate bipolar transistor (IGBT) failures in factory tests on a prototype 1500-kW DFIG. Following the failure, the vector-controlled DFIG was monitored closely, and in a 4-h period, it was found that the incremental encoder picked up extraneous noise four times in the reset "Z pulse" and the hardware PLL recorded ten errors. The wrong angular measurements mean that the *d*–*q* reference frames of the stator and the rotor will become misaligned. This leads to: 1) the DFIG perceiving wrong *P*–*Q* reference settings, resulting in very large steady-state destructive currents and 2) system instability also leads to large destructive currents. This paper presents the analyses

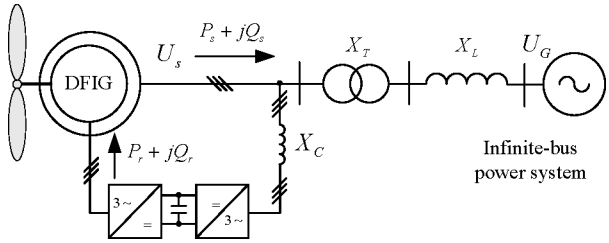

Fig. 1. Schematic of DFIG-based wind power generation system.

of the causes of failure, and the verification by simulations and experimental tests.

Section II describes the sources of erroneous angular measurements. Section III presents the mathematical model of the vector-controlled DFIG for measurement error analyses. In the event of failure due to instability, the analysis requires examination of two feedback loops. Section IV treats the case of inner loop (current) feedback. Then, the analysis proceeds to the outer loop (complex power *P–Q*) feedback in Section V. Section VI presents experimental results, which show that erroneous measurement frequently leads to failure from instability. Section VII offers a method of preventing erroneous measurements.

II. Sources of Errors in Angular Measurements

The DFIG controller is usually implemented by digital signal processors (DSPs) or field-programmable gate arrays (FPGA), whose interface voltage is often a low voltage of 3.3 V. These components are easily affected by temperature change and electromagnetic interference.

A. Position Encoder

Although there is a growing literature on sensorless DFIG control [6], [7], the majority of wind turbine generators make use of incremental position encoder. The signals of commonly used incremental encoder are: two-phase incremental signals A and B, and an index signal Z. The A and B signals are used to count the rotor position and Z pulse is used to reset the counter. The Z pulse has a short duration, and therefore, it is easily contaminated by external noise pickup.

Fig. 2 illustrates the operation of an incremental position encoder. As the shaft rotates, its mechanical angular position is depicted as shown Fig. 2(b). In a four-pole DFIG, the rotor electrical angle is as shown in Fig. 2(c). The measured rotor angle θ_r shown in Fig. 2(d) is reset at π or when the Z pulse shown in Fig. 2(a) appears. Normally, the Z pulse appears when the mechanical angle reaches 2π, as illustrated in Fig. 2(b).

Fig. 2(a) shows an incident when an external disturbance is mistaken for a Z pulse. Fig. 2(d) shows that the mistaken Z pulse leads to wrong measured electrical angle in two subperiods. The mistake is corrected after one full mechanical period.

There is also the possibility that the Z pulse is missed. But this is not serious because the electrical angle counter can be automatically reset when it reaches π in the program.

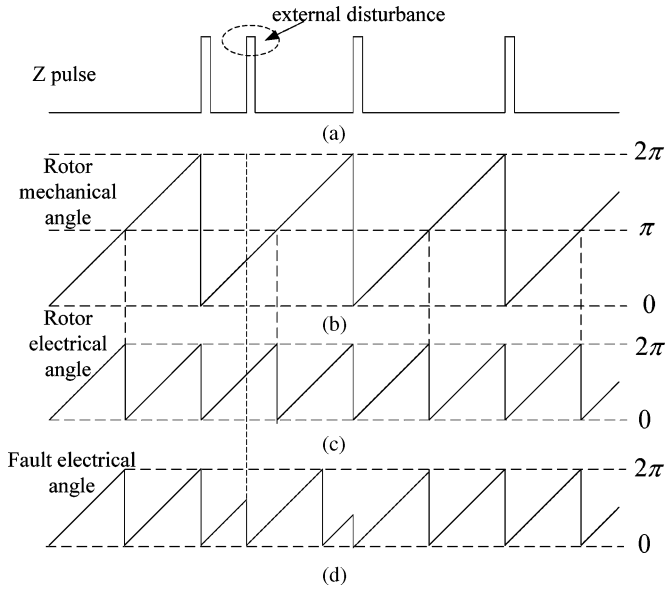

Fig. 2. Operation of incremental position encoder and influence of external disturbance on Z pulse.

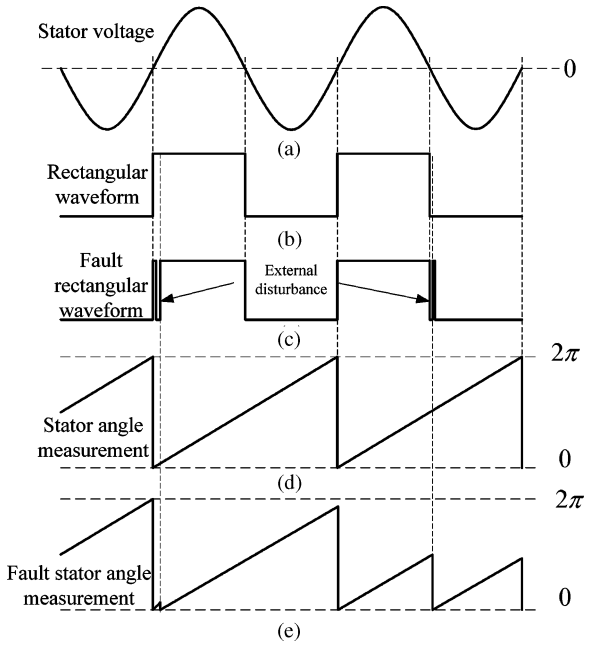

Fig. 3. Operation of hardware PLL and consequence of erroneous detection of zero crossover.

B. Hardware PLL

Hardware PLL is an easy way to get the angle information of the voltage, and it is widely used in power electronic applications. The stator flux angle, which is used in the control strategy, can be easily calculated from the stator angle captured by the hardware. One implementation of the hardware PLL is illustrated in Fig. 3.

As shown in Fig. 3(a), the rising edge and descending edge of the zero-crossing point of the stator voltage waveform is detected by a comparator and converted into a rectangular waveform, as shown in Fig. 3(b). The correct stator angle θ_s shown

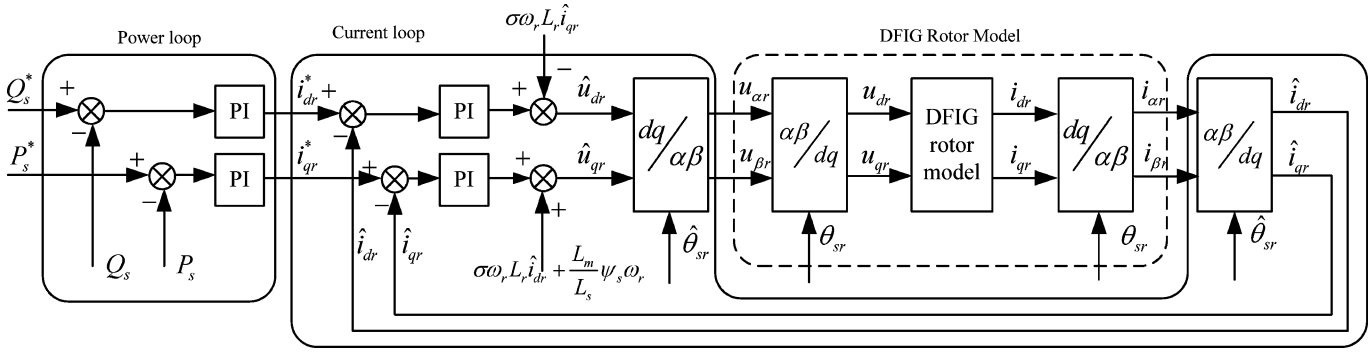

Fig. 4. Model and vector control scheme of DFIG.

in Fig. 3(d) is measured by counting the clocking pulses within the two rising edges of the rectangular waveforms of Fig. 3(b).

Very low pickup noise in the stator voltage easily falsifies the exact location of a zero crossover. Fig. 3(c) illustrates the situation when an external disturbance occurs near one rising zero-voltage crossover resulting in a small error, as shown in Fig. 3(e). Fig. 3(c) also shows the case of an external disturbance close to the descending zero-voltage crossover. Fig. 3(e) shows that the error in the angle measurement θ_s is more serious in wrongly detecting the descending zero-voltage crossover.

III. Model of DFIG Control System for Angle Measurement Error Analysis

For measurement error analysis, the schematic of a DFIG under vector control, as shown in Fig. 4, has been developed. The DFIG is represented by the DFIG model block. (The transformations from the original three-phase *a–b–c* frame to the α–β–0 frame and its inverse have been omitted. Section A summarizes the equations of the DFIG.)

In vector control, the power loop block receives the complex power references Q_s^*, P_s^*, and sends out rotor current commands i_{dr}^*, i_{qr}^*. But the DFIG is controlled by rotor voltages from the rotor-side converter. In order to implement the current commands, the current loop block sends voltage commands u_{dr}, u_{qr} to the DFIG and applies negative feedback to ensure that the rotor commands are obtained.

Section II describes how the measurements from the position encoder and the PLL are introduced for failure analysis. In the physical DFIG, the correct stator–rotor angle relationship of the physical machine is represented by θ_{sr}. As illustrated in Fig. 4, the $\alpha\beta/dq$ transformation block and its inverse transformation block inside the DFIG model make use of θ_{sr}. The measurement angle is $\hat{\theta}_{sr}$, which can be erroneous. The errors enter the system analysis in the $\alpha\beta/dq$ transformation block and its inverse transformation block outside the DFIG model.

A. DFIG Model

The voltage equations of the DFIG in the arbitrary *d–q* reference frame are (stator in the generator convention and rotor in the motor convention)

$$\begin{cases} u_{ds} = -r_s i_{ds} + p\psi_{ds} - \psi_{qs}\omega_s \\ u_{qs} = -r_s i_{qs} + p\psi_{ds} + \psi_{ds}\omega_s \\ u_{dr} = r_r i_{dr} + p\psi_{dr} - \psi_{qr}\omega_r \\ u_{qr} = r_r i_{qr} + p\psi_{qr} + \psi_{dr}\omega_r. \end{cases} \tag{1}$$

The corresponding flux linkages are

$$\begin{cases} \psi_{ds} = -L_s i_{ds} + L_m i_{dr} \\ \psi_{qs} = -L_s i_{qs} + L_m i_{qr} \\ \psi_{dr} = L_r i_{dr} - L_m i_{ds} \\ \psi_{qr} = L_r i_{qr} - L_m i_{qs}. \end{cases} \tag{2}$$

The stator resistance is relatively very small. For large power rating, it is less than 1% of the stator reactance. For simplicity, the stator resistance is neglected.

In decoupled *P–Q* control, the transformation angle θ_{sr} is found so that the rotor *d–q* axes aligned with the stator *d–q* flux linkage axes, which means $\psi_{ds} = \psi_s$ and $\psi_{qs} = 0$. Since the stator resistance is neglected, the stator voltage can be expressed as

$$\begin{cases} u_{ds} = 0 \\ u_{qs} = \psi_s\omega_s = u_s. \end{cases} \tag{3}$$

The stator flux axis and the rotor flux axis are aligned only when the PLL and the position encoder measure the angles θ_s and θ_r correctly.

The equations of the stator and rotor currents are

$$\begin{cases} i_{ds} = \dfrac{L_m}{L_s} i_{dr} - \dfrac{\psi_s}{L_s} \\ i_{qs} = \dfrac{L_m}{L_s} i_{qr}. \end{cases} \tag{4}$$

By substituting (2) into (1), the rotor voltage equations are as follows:

$$\begin{cases} u_{dr} = (r_r + L_r\sigma p) i_{dr} - \sigma\omega_r L_r i_{qr} \\ u_{qr} = (r_r + L_r\sigma p) i_{qr} + \sigma\omega_r L_r i_{dr} + \dfrac{L_m}{L_s}\psi_s\omega_r \end{cases} \tag{5}$$

where $\sigma = (L_s L_r - L_m^2)/L_s L_r$ is the leakage factor. Taking the rotor *d–q* axes currents as state variables, the state equations

can be written as

$$p\begin{bmatrix} i_{dr} \\ i_{qr} \end{bmatrix} = \mathbf{A}\begin{bmatrix} i_{dr} \\ i_{qr} \end{bmatrix} + \mathbf{B}\begin{bmatrix} u_{dr} \\ u_{qr} \end{bmatrix} + \mathbf{D} \tag{6}$$

with

$$\mathbf{A} = \begin{bmatrix} -\dfrac{r_r}{\sigma L_r} & \omega_r \\ -\omega_r & -\dfrac{r_r}{\sigma L_r} \end{bmatrix},\ \mathbf{B} = \frac{1}{\sigma L_r}\mathbf{I}_{2\times 2},$$

$$\mathbf{D} = \begin{bmatrix} 0 \\ -\dfrac{L_m}{L_s}\psi_s\omega_r \end{bmatrix}.$$

B. Modeling Measurement Errors

The critical angle of DFIG control design is the slip angle

$$\theta_{sr} = \theta_s - \theta_r \tag{7}$$

where θ_s and θ_r are measured by the PLL and the position encoder.

Inside the DFIG model, the $\alpha\beta/dq$ transformation block and its inverse transformation block implement the transformation

$$\begin{bmatrix} i_{\alpha r} \\ i_{\beta r} \end{bmatrix} = \begin{bmatrix} \cos\theta_{sr} & -\sin\theta_{sr} \\ \sin\theta_{sr} & \cos\theta_{sr} \end{bmatrix}\begin{bmatrix} i_{dr} \\ i_{qr} \end{bmatrix} \tag{8}$$

$$\begin{bmatrix} u_{dr} \\ u_{qr} \end{bmatrix} = \begin{bmatrix} \cos\theta_{sr} & \sin\theta_{sr} \\ -\sin\theta_{sr} & \cos\theta_{sr} \end{bmatrix}\begin{bmatrix} u_{\alpha r} \\ u_{\beta r} \end{bmatrix}. \tag{9}$$

Either the PLL measurement of θ_s or the incremental encoder measurement of rotor angle θ_r can introduce an angle deviation in the slip angle. In the following sections, the sources of the disturbances will not be distinguished. The actual and observed slip angles are represented as θ_{sr} and $\hat{\theta}_{sr}$, respectively. The slip angle deviation can be written as

$$\Delta\theta_{sr} = \theta_{sr} - \hat{\theta}_{sr}. \tag{10}$$

If there is an error in the angular measurements, it is introduced in the $\alpha\beta/dq$ transformation of the rotor currents, thereby leading to erroneous $[\hat{i}_{dr}, \hat{i}_{qr}]^T$

$$\begin{bmatrix} \hat{i}_{dr} \\ \hat{i}_{qr} \end{bmatrix} = \begin{bmatrix} \cos\hat{\theta}_{sr} & \sin\hat{\theta}_{sr} \\ -\sin\hat{\theta}_{sr} & \cos\hat{\theta}_{sr} \end{bmatrix}\begin{bmatrix} i_{\alpha r} \\ i_{\beta r} \end{bmatrix}. \tag{11}$$

Likewise, in the current loop block, it leads to erroneous command voltages $[\hat{u}_{dr}, \hat{u}_{qr}]^T$

$$\begin{bmatrix} u_{\alpha r} \\ u_{\beta r} \end{bmatrix} = \begin{bmatrix} \cos\hat{\theta}_{sr} & -\sin\hat{\theta}_{sr} \\ \sin\hat{\theta}_{sr} & \cos\hat{\theta}_{sr} \end{bmatrix}\begin{bmatrix} \hat{u}_{dr} \\ \hat{u}_{qr} \end{bmatrix}. \tag{12}$$

Substituting (11) into (8) and (12) into (9), together with (10), the relations between the observed and actual values of *d–q* axes components can be expressed as

$$\begin{bmatrix} \hat{i}_{dr} \\ \hat{i}_{qr} \end{bmatrix} = \mathbf{T}\begin{bmatrix} i_{dr} \\ i_{qr} \end{bmatrix} \tag{13}$$

$$\begin{bmatrix} u_{dr} \\ u_{qr} \end{bmatrix} = \mathbf{T}^{-1}\begin{bmatrix} \hat{u}_{dr} \\ \hat{u}_{qr} \end{bmatrix} \tag{14}$$

where

$$\mathbf{T} = \begin{bmatrix} \cos\Delta\theta_{sr} & -\sin\Delta\theta_{sr} \\ \sin\Delta\theta_{sr} & \cos\Delta\theta_{sr} \end{bmatrix}$$

$$\mathbf{T}^{-1} = \begin{bmatrix} \cos\Delta\theta_{sr} & \sin\Delta\theta_{sr} \\ -\sin\Delta\theta_{sr} & \cos\Delta\theta_{sr} \end{bmatrix}.$$

Substituting (13) and (14) into (6), the DFIG equations can be rewritten as

$$\begin{bmatrix} \hat{i}_{dr} \\ \hat{i}_{qr} \end{bmatrix} = \mathbf{T}\mathbf{A}\mathbf{T}^{-1}\begin{bmatrix} \hat{i}_{dr} \\ \hat{i}_{qr} \end{bmatrix} + \mathbf{T}\mathbf{B}\mathbf{T}^{-1}\begin{bmatrix} \hat{u}_{dr} \\ \hat{u}_{qr} \end{bmatrix} + \mathbf{T}\mathbf{D}. \tag{15}$$

The mechanical equation of motion can be expressed as

$$Jp\omega_m = T_m - T_{em}. \tag{16}$$

In the wind power application, the turbine inertia is relatively large, usually a few seconds. The dynamics of the power electronic converter is relatively fast, usually a few microseconds. For this reason, the rotor angular frequency ω_m and the slip angular frequency ω_r are considered as constants in the following sections.

Since the stator of DFIG is connected to the power grid, the magnitude and frequency of the stator voltage (in the *d–q* frame) can be seen as constants in normal operation. In the following sections, the stator voltage u_s and the corresponding stator flux linkage ψ_s are treated as constants.

IV. Stability Analysis With Current Loop Only

In order to understand how errors in angle measurement lead to IGBT destruction, this section describes the small-signal stability analysis of the system shown in Fig. 4 when there is the current loop feedback only.

A. Derivation of State Matrix

The state equations of the *d–q* axes current controller can be written as

$$\begin{cases} px_1^c = i_{dr}^* - \hat{i}_{dr} \\ \hat{u}_{dr} = k_{i1}^c x_1^c - k_{p1}^c\hat{i}_{dr} + k_{p1}^c i_{dr}^* - \sigma\omega_r L_r\hat{i}_{qr} \end{cases} \tag{17}$$

$$\begin{cases} px_2^c = i_{qr}^* - \hat{i}_{qr} \\ \hat{u}_{qr} = k_{i2}^c x_2^c - k_{p2}^c\hat{i}_{qr} + k_{p2}^c i_{qr}^* + \sigma\omega_r L_r\hat{i}_{dr} + \dfrac{L_m}{L_s}\psi_s\omega_r \end{cases} \tag{18}$$

where x_1^c and x_2^c are the two state variables, k_{p1}^c and k_{p2}^c are the proportional gains, and k_{i1}^c and k_{i2}^c are the integrating gains. Writing (17) and (18) in matrix form, one can get

$$p\begin{bmatrix} x_1^c \\ x_2^c \end{bmatrix} = -\mathbf{I}_{2\times 2}\begin{bmatrix} \hat{i}_{dr} \\ \hat{i}_{qr} \end{bmatrix} + \mathbf{I}_{2\times 2}\begin{bmatrix} i_{dr}^* \\ i_{qr}^* \end{bmatrix} \tag{19}$$

$$\begin{bmatrix} \hat{u}_{dr} \\ \hat{u}_{qr} \end{bmatrix} = \mathbf{K}_i^c\begin{bmatrix} x_1^c \\ x_2^c \end{bmatrix} + \tilde{\mathbf{K}}_p^c\begin{bmatrix} \hat{i}_{dr} \\ \hat{i}_{qr} \end{bmatrix} + \mathbf{K}_p^c\begin{bmatrix} i_{dr}^* \\ i_{qr}^* \end{bmatrix} + \mathbf{D} \tag{20}$$

$$\mathbf{K}_i^c = \begin{bmatrix} k_{i1}^c & 0 \\ 0 & k_{i2}^c \end{bmatrix} \quad \tilde{\mathbf{K}}_p^c = \begin{bmatrix} -k_{p1}^c & -\sigma\omega_r L_r \\ \sigma\omega_r L_r & -k_{p2}^c \end{bmatrix}$$

$$\mathbf{K}_p^c = \begin{bmatrix} k_{p1}^c & 0 \\ 0 & k_{p2}^c \end{bmatrix}.$$

Substituting (20) into (15), one can get

$$p\begin{bmatrix} \hat{i}_{dr} \\ \hat{i}_{qr} \end{bmatrix} = (\mathbf{TAT}^{-1} + \mathbf{TBT}^{-1}\tilde{\mathbf{K}}_p^c)\begin{bmatrix} \hat{i}_{dr} \\ \hat{i}_{qr} \end{bmatrix} + \mathbf{TBT}^{-1}\mathbf{K}_i^c\begin{bmatrix} x_1^c \\ x_2^c \end{bmatrix} + \mathbf{TBT}^{-1}\mathbf{K}_p^c\begin{bmatrix} i_{dr}^* \\ i_{qr}^* \end{bmatrix} + \mathbf{TBT}^{-1}\mathbf{D} + \mathbf{TD}. \quad (21)$$

Combining (19) and (21) together, a fourth-order system can be built and the new state variables of the system are $x = [\,\hat{i}_{dr} \quad \hat{i}_{qr} \quad x_1^c \quad x_2^c\,]^T$, and the new 4×4 state matrix of the whole system can be expressed as

$$\mathbf{A}^c = \begin{bmatrix} \mathbf{TAT}^{-1} + \mathbf{TBT}^{-1}\tilde{\mathbf{K}}_p^c & \mathbf{TBT}^{-1}\mathbf{K}_i^c \\ -\mathbf{I}_{2\times 2} & \mathbf{0} \end{bmatrix}. \quad (22)$$

Making the proportional and integrating gains of the two current loops equal $k_{p1}^c = k_{p2}^c = k_p^c$ and $k_{i1}^c = k_{i2}^c = k_i^c$, the matrix $\mathbf{A}^c$ simplifies to

$$\mathbf{A}^c = \begin{bmatrix} \mathbf{TAT}^{-1} + \mathbf{TBT}^{-1}\tilde{\mathbf{K}}_p^c & k_i^c\mathbf{TBT}^{-1} \\ -\mathbf{I}_{2\times 2} & \mathbf{0} \end{bmatrix}. \quad (23)$$

Substituting $\mathbf{A}$, $\mathbf{B}$, $\mathbf{T}$, $\mathbf{T}^{-1}$, $\tilde{\mathbf{K}}_p^c$, K_i^c, and $\mathbf{I}_{2\times 2}$, the complete form of $\mathbf{A}^c$ simplifies to

$$\mathbf{A}^c = \begin{bmatrix} -\dfrac{r_r + k_p^c}{\sigma L_r} & 0 & \dfrac{k_i^c}{\sigma L_r} & 0 \\ 0 & -\dfrac{r_r + k_p^c}{\sigma L_r} & 0 & \dfrac{k_i^c}{\sigma L_r} \\ -1 & 0 & 0 & 0 \\ 0 & -1 & 0 & 0 \end{bmatrix}. \quad (24)$$

B. Stability Analysis

It can be seen from (24) that the matrix $\mathbf{A}^c$ contains no term related to $\Delta\theta_{sr}$. That is to say that the angle deviation will not affect the $\mathbf{A}^c$ matrix of the system with the current loop only.

The determinant of the transfer function of the matrix $\mathbf{A}^c$ is

$$G^c(s) = |s\mathbf{I}_{4\times 4} - \mathbf{A}^c| = s^4 + 2as^3 + (a^2 + 2b)s^2 + 2abs + b^2 = 0 \quad (25)$$

where $a = r_r + k_p^c/\sigma L_r$ and $b = k_i^c/\sigma L_r$. From the Routh's criterion on the fourth-order polynomial of $G^c(s)$, the system is stable when $a > 0$ and $b > 0$ irrespective of what current controller parameters are used.

C. Simulations

Although errors in the angle measurement do not affect system stability, it still can cause undesirably large stator and rotor currents, which have negative effect on the operation of the system.

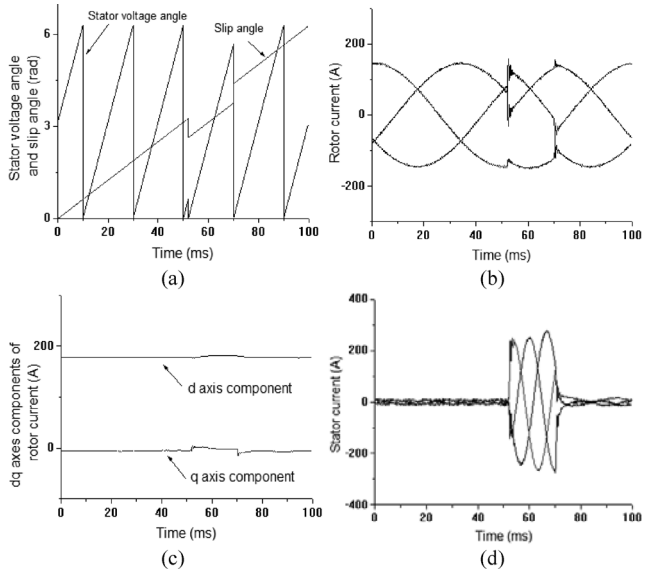

Fig. 5. Simulation results with the current loop only (angle deviation = 0.628). (a) Stator voltage and slip angle. (b) *a–b–c* rotor current. (c) *d–q* axes components of rotor current. (d) a–b–c stator current.

In order to verify the results in the previous section, two simulations have been carried out using power system computer aided design (PSCAD), an industry grade simulation software. The DFIG is operated so that the rotor speed is 0.8 of the synchronous speed, and the operating rotor *d*-axis current is 180 A and the *q*-axis current is 0 A. In this situation, the rotor current is equal to the no-load excitation current, and the stator active and reactive powers are nearly zero.

In the following simulation and experiment, the angle deviation on the stator voltage angle was taken as the examples. It has to be noted that the angle deviation of the rotor angle has the similar effect on the system response, which is decided by the magnitude of the slip angle deviation.

Fig. 5 shows the simulation waveforms when the PLL has a small angle deviation of 0.628 rad. Fig. 5(a) shows the stator angle and the slip angle from the PLL measurement. Fig. 5(b) and (c) shows the waveforms of the three-phase *a—b–c* rotor currents and the rotor current in the *d–q* frame, respectively. Fig. 5(d) shows the three-phase *a–b–c* stator currents.

Fig. 6 shows the waveforms in an identical simulation result, with the difference that the angle deviation is a large angle error of 3.14 rad.

Although the fault current shown in Fig. 6(d) is larger than that shown in Fig. 5(d), one has also taken into account of the duration of the fault. But no matter how much the angle deviation is, the system can still kept stable. The peak value of the stator current shown in Fig. 6 is about 800 A.

Since the PLL resets when the count reaches 2π electrical radians, the error is contained within one cycle of the 50 Hz.

V. Stability Analysis With Power Outer Loops

The analysis of this section includes the outer power feedback loop shown in Fig. 4.

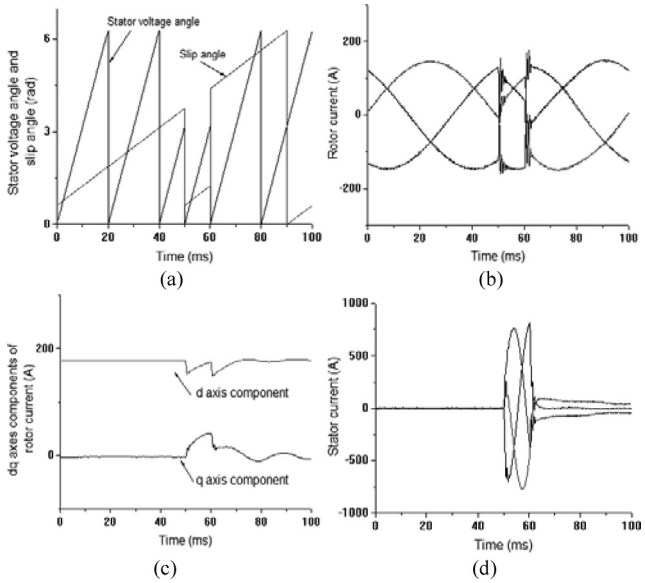

Fig. 6. Simulation results with the current loop only (angle deviation = 3.14). (a) Stator voltage and slip angle. (b) *a–b–c* rotor current. (c) *d–q* axes components of rotor current. (d) *a–b–c* stator current.

A. Modeling of the Power Loop With DFIG

In order to control the stator active and reactive powers, a power outer loop is often added to the current loop reference. The formulas of the stator active and reactive powers are

$$\begin{cases} P_s = u_{ds} i_{ds} + u_{qs} i_{qs} \\ Q_s = u_{qs} i_{ds} - u_{ds} i_{qs}. \end{cases} \tag{26}$$

Substituting (3) and (4) into (26), the stator active and reactive powers can be represented as

$$\begin{cases} P_s = \dfrac{L_m}{L_s} u_s i_{qr} \\ Q_s = \dfrac{L_m}{L_s} u_s i_{dr} + \dfrac{\psi_s u_s}{L_s}. \end{cases} \tag{27}$$

The state equations of the active and reactive power controllers can be written as

$$\begin{cases} p x_1^p = Q_s^* - Q_s \\ i_{dr}^* = k_{i1}^p x_1^p - k_{p1}^p Q_s + k_{p1}^p Q_s^* \end{cases} \tag{28}$$

$$\begin{cases} p x_2^p = P_s^* - P_s \\ i_{qr}^* = k_{i2}^p x_2^p - k_{p2}^p P_s + k_{p2}^p P_s^* \end{cases} \tag{29}$$

where x_1^p and x_2^p are two new state variables. The proportional gain constants inside the power loop block shown in Fig. 4 are k_{p1}^p and k_{p2}^p, and the integral gains are k_{i1}^p and k_{i2}^p. Substituting (13) and (27) into (28) and (29), the state equations can be expressed as

$$p \begin{bmatrix} x_1^p \\ x_2^p \end{bmatrix} = -\mathbf{K}_m \mathbf{T}^{-1} \begin{bmatrix} \hat{i}_{dr} \\ \hat{i}_{qr} \end{bmatrix} + \mathbf{I}_{2\times 2} \begin{bmatrix} Q_s^* \\ P_s^* \end{bmatrix} + \mathbf{D}^p \tag{30}$$

$$\begin{bmatrix} i_{dr}^* \\ i_{qr}^* \end{bmatrix} = \mathbf{K}_i^p \begin{bmatrix} x_1^p \\ x_2^p \end{bmatrix} - \mathbf{K}_p^p \mathbf{K}_m \mathbf{T}^{-1} \begin{bmatrix} \hat{i}_{dr} \\ \hat{i}_{qr} \end{bmatrix} + \mathbf{K}_p^p \begin{bmatrix} Q_s^* \\ P_s^* \end{bmatrix} + \mathbf{K}_p^p \mathbf{D}^p \tag{31}$$

where

$$\mathbf{K}_i^p = \begin{bmatrix} k_{i1}^p & 0 \\ 0 & k_{i2}^p \end{bmatrix}, \ \mathbf{K}_p^p = \begin{bmatrix} k_{p1}^p & 0 \\ 0 & k_{p2}^p \end{bmatrix},$$

$$\mathbf{K}_m = k_m \mathbf{I}_{2\times 2}, \ k_m = \frac{L_m}{L_s} u_s, \quad \mathbf{D}^p = \begin{bmatrix} -\dfrac{\psi_s u_s}{L_s} \\ 0 \end{bmatrix}$$

Combining (19), (21), (30), and (31) together, a sixth-order state vector $x = [\,\hat{i}_{dr} \quad \hat{i}_{qr} \quad x_1^c \quad x_2^c \quad x_1^p \quad x_2^p\,]^T$ can be built with a new 6×6 state matrix, (32), as shown at the bottom of the page.

Assuming $k_{p1}^p = k_{p2}^p = k_p^p$ and $k_{i1}^p = k_{i2}^p = k_i^p$, $\mathbf{A}^p$ can be simplified, (33), as shown at the bottom of the page.

Substituting the submatrices defined earlier, $\mathbf{A}^p$ takes the completed form as

$$\mathbf{A}^p = \begin{bmatrix} -a & -b & g & 0 & h & 0 \\ b & -a & 0 & g & 0 & h \\ -c & -d & 0 & 0 & i & 0 \\ d & -c & 0 & 0 & 0 & i \\ -e & -f & 0 & 0 & 0 & 0 \\ f & -e & 0 & 0 & 0 & 0 \end{bmatrix} \tag{34}$$

where

$$a = \frac{r_r + k_p^c}{\sigma L_r} + \frac{k_m k_p^c k_p^p}{\sigma L_r} \cos\Delta\theta_{sr}, \ b = \frac{k_m k_p^c k_p^p}{\sigma L_r} \sin\Delta\theta_{sr},$$

$$c = 1 + k_m k_p^p \cos\Delta\theta_{sr}, \ d = k_m k_p^p \sin\Delta\theta_{sr},$$

$$e = k_m \cos\Delta\theta_{sr}, \ f = k_m \sin\Delta\theta_{sr}, \ g = \frac{k_i^c}{\sigma L_r},$$

$$h = \frac{k_p^c k_i^p}{\sigma L_r}, \quad i = k_i^p.$$

$$\mathbf{A}^p = \begin{bmatrix} \mathbf{T}\mathbf{A}\mathbf{T}^{-1} + \mathbf{T}\mathbf{B}\mathbf{T}^{-1}\tilde{\mathbf{K}}_p^c - k_p^c k_m \mathbf{T}\mathbf{B}\mathbf{T}^{-1}\mathbf{K}_p^p\mathbf{T}^{-1} & k_i^c \mathbf{T}\mathbf{B}\mathbf{T}^{-1} & k_p^c \mathbf{T}\mathbf{B}\mathbf{T}^{-1}\mathbf{K}_i^p \\ -(\mathbf{I}_{2\times 2} + k_m \mathbf{K}_p^p \mathbf{T}^{-1}) & \mathbf{0} & \mathbf{K}_i^p \\ -\mathbf{K}_m \mathbf{T}^{-1} & \mathbf{0} & \mathbf{0} \end{bmatrix}. \tag{32}$$

$$\mathbf{A}^p = \begin{bmatrix} \mathbf{T}\mathbf{A}\mathbf{T}^{-1} + \mathbf{T}\mathbf{B}\mathbf{T}^{-1}\tilde{\mathbf{K}}_p^c - k_p^c k_p^p k_m \mathbf{T}\mathbf{B}\mathbf{T}^{-1}\mathbf{T}^{-1} & k_i^c \mathbf{T}\mathbf{B}\mathbf{T}^{-1} & k_p^c k_i^p \mathbf{T}\mathbf{B}\mathbf{T}^{-1} \\ -(\mathbf{I}_{2\times 2} + k_p^p k_m \mathbf{T}^{-1}) & \mathbf{0} & k_i^p \mathbf{I}_{2\times 2} \\ -k_m \mathbf{T}^{-1} & \mathbf{0} & \mathbf{0} \end{bmatrix}. \tag{33}$$

TABLE I
DAMPING RATIO AND FREQUENCY OF EIGENVALUES

Eigenvalue	Damping ratio	Frequency (rad/s)
$\Delta\theta_{sr} = 0.1$		
$\lambda_{1,2} = -30.9 \pm j1.07$	1	30.9
$\lambda_{3,4} = -0.13 \,\&\, -0.24$	1	0.13&0.24
$\lambda_{5,6} = -0.407 \pm j4.89e^{-3}$	1	0.407
$\Delta\theta_{sr} = 3$		
$\lambda_{1,2} = -6.11 \pm j1.39$	0.975	6.27
$\lambda_{3,4} = 0.78 \pm j0.39$	-0.895	0.871
$\lambda_{5,6} = -0.408 \pm j1.85e^{-3}$	1	0.408

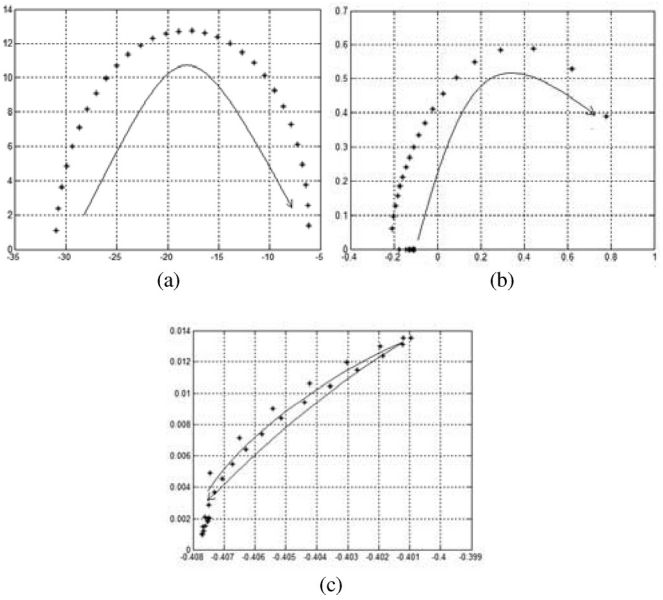

Fig. 7. Plots of eigenvalues as $\Delta\theta_{sr}$ increases from 0.1 to 3.0. (a) λ_1. (b) λ_3. (c) λ_5.

B. Stability Analysis

The formulas of a, b, c, d, e, and f of (34) contain trigonometric functions of $\Delta\theta_{sr}$. Therefore, $\Delta\theta_{sr}$ affect the positions of the eigenvalues of the matrix $\mathbf{A}^p$ in the complex s-plane. The system becomes unstable when any eigenvalue or complex conjugate pair lies on the right-hand side of the imaginary axis.

The eigenvalues of the matrix $\mathbf{A}^p$ can be divided into three groups: $\lambda_{1,2}$ are related to the rotor current, $\lambda_{3,4}$ are related to the rotor current controller, and $\lambda_{5,6}$ are related to the active and reactive power controllers.

Using the system parameters listed in Appendix B, the damping ratio and frequency of each complex conjugate pair of eigenvalues are listed in Table I for $\Delta\theta_{sr} = 0.1$ and $\Delta\theta_{sr} = 3$. The eigenvalues, as $\Delta\theta_{sr}$ varies from $\Delta\theta_{sr} = 0.1$ to $\Delta\theta_{sr} = 3$, are plotted in Fig. 7, with the solid arrow indicating the direction of increase of $\Delta\theta_{sr}$.

It can be seen from Table I and Fig. 7 that when $\Delta\theta_{sr}$ is 0.1, all the modes are positively damped. But when $\Delta\theta_{sr}$ increases, $\lambda_{3,4}$ has moved to the right half of the complex s-plane before reaching $\Delta\theta_{sr} = 3$, indicating that the system will have become unstable.

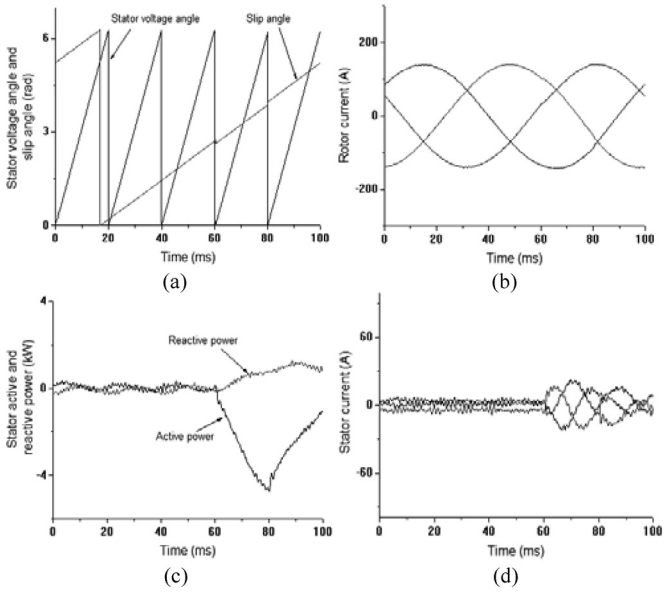

Fig. 8. Simulation results with the power outer loop (angle deviation $\Delta\theta_{sr} = 0.1$). (a) Stator voltage and slip angle. (b) *a–b–c* rotor current. (c) Stator active and reactive powers. (d) *a–b–c* stator current.

The reason why the inner current loop feedback is transparent to $\Delta\theta_{sr}$ and therefore does not lead to instability can be seen in Fig. 4. The error in $\hat{\theta}_{sr}$ in the $\alpha\beta/dq$ transformation *immediately after* the DFIG model block is cancelled by the $dq/\alpha\beta$ transformation *immediately before*.

In contrast, the power loop accepts as feedback signals (P_s,Q_s), which, from (27), contain ($\hat{i}_{qr}$, $\hat{i}_{dr}$) that have the error $\Delta\theta_{sr}$.

It should not be forgotten that the formulas of a, b, c,..., i of (34) are also determined by system parameters and gain constants. They affect the placement of the eigenvalues of the matrix $\mathbf{A}^p$, but the designer would have tuned the gains for stable operation.

C. Simulations

The two results of simulations, which are presented here as Figs. 8 and 9, are patterned after Figs. 5 and 6, respectively. The intent is to allow comparison of the effect of closing the outer power loop and for comparison of the effect of small angular error $\Delta\theta_{sr} = 0.1$ rad and large error $\Delta\theta_{sr} = 3.14$ rad.

As shown in Figs. 5 and 6, the source of $\Delta\theta_{sr}$ is from a hardware PLL and the rotor speed is 0.8 of the synchronous speed. The power references of the stator active and reactive powers are both set to zero. The waveforms are:

1) stator angle and slip angle deviation;
2) rotor currents;
3) active and reactive powers; and
4) stator currents.

It can be seen from Fig. 8 that when the angle deviation is $\Delta\theta_{sr} = 0.1$, the system is still stable although there is a surge in the stator currents shown in Fig. 8(d). But it is followed by

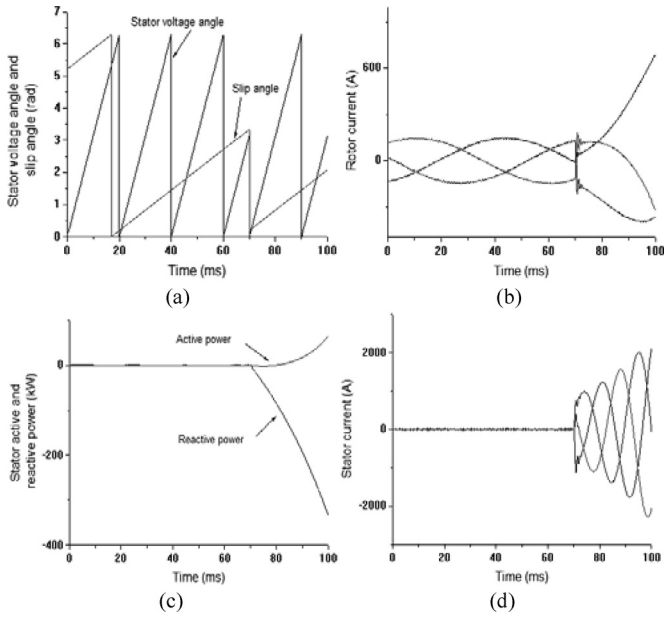

Fig. 9. Simulation results with the power outer loop (angle deviation $\Delta\theta_{sr} = 3.14$). (a) Stator voltage and slip angle. (b) *a–b–c* rotor current. (c) Stator active and reactive powers. (d) *a–b–c* stator current.

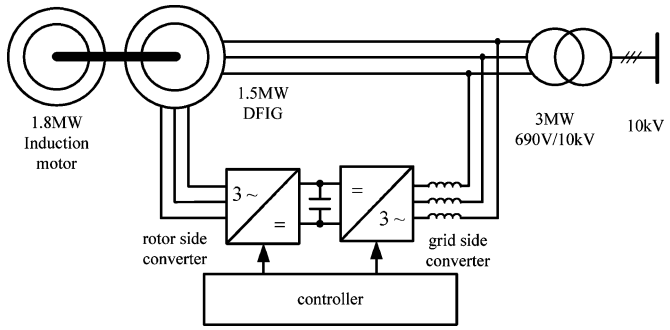

Fig. 10. Experiment setup of the 1.5-MW DFIG experiment platform.

exponential decay that in this situation, all the eigenvalues of the system are still located at the left half of the complex *s*-plane.

Fig. 9 shows the simulation results for $\Delta\theta_{sr} = 3.14$. The waveforms of Fig. 8(b)–(d) show exponential growth related to eigenvalues having moved to the right half of the complex *s*-plane.

VI. Experiment

The experimental results reported here have been measured from an experimental platform set up to test DFIG of 1.5 MW rating for wind power generation. The problems mentioned in this paper were observed experimentally in long-duration tests from this platform. The cure of the problems, which is described in the next section, is also proven experimentally in this platform.

A. Experiment Setup

The diagram of the 1.5-MW DFIG experiment platform is shown in Fig. 10.

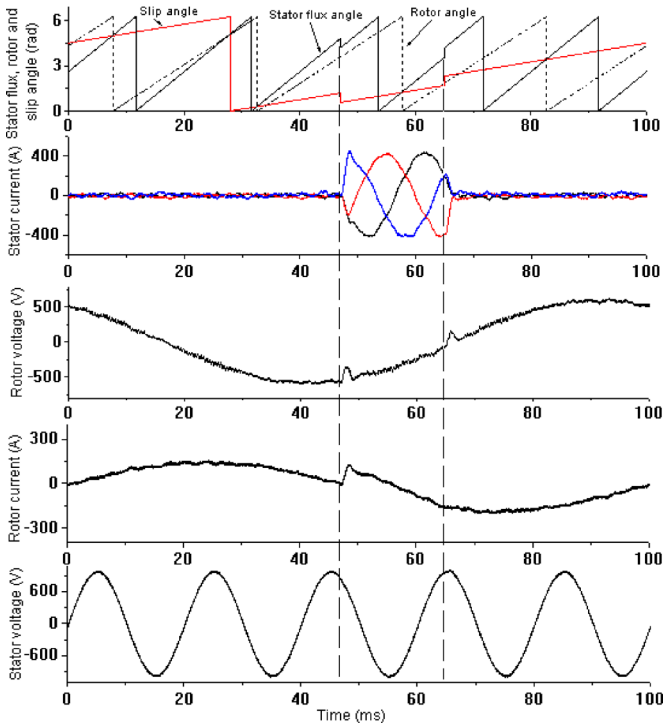

Fig. 11. Experiment result with current loop only (angle deviation $\Delta\theta_{sr} = 0.628$).

The experiment setup comprises the following parts.

1) A 1.5-MW DFIG. Its parameters (listed in Appendix A) are used in simulation studies.
2) The prime mover to drive the DFIG is a 1.8-MW induction motor controlled by a variable frequency converter.
3) A 3-MVA transformer connects the DFIG to the 10-kV power grid.
4) The grid-side converter and the rotor-side converter to control the active and reactive powers of DFIG. The power rating of the grid-side converter is 400 kW, while the power rating of the rotor side converter is 650 kVA. The switching frequency of the grid-side and rotor-side converters is 3 kHz.
5) The control schemes were implemented in two DSPs. The rotor speed and position signals are obtained via an incremental encoder. The hardware PLL is used to measure the stator angle. The sampling time of the controller is 5 kHz. The controller's parameters are listed in Appendix B. The natural closed-loop frequency for the current controller is 86.6 rad/s.

B. Experiment Result With Current Loop only

In this section, the control strategy is implemented with the current loop only. The reference of the rotor current was equal to the no-load excitation current, so the stator active power and reactive powers were very small. During the tests, the rotor speed was 0.8 of the synchronous speed. Two tests were performed and the waveforms are shown in Figs. 11 and 12.

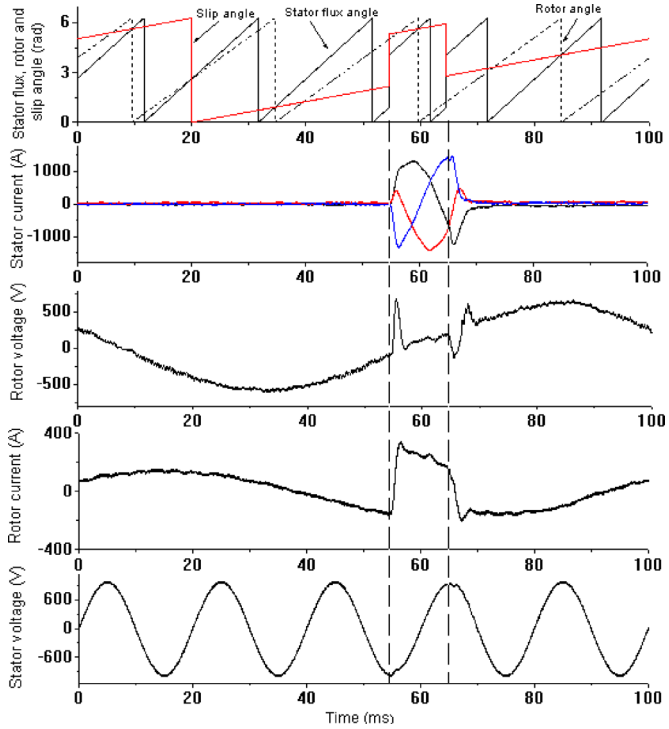

Fig. 12. Experiment result with current loop only (angle deviation $\Delta\theta_{sr} = 3.14$).

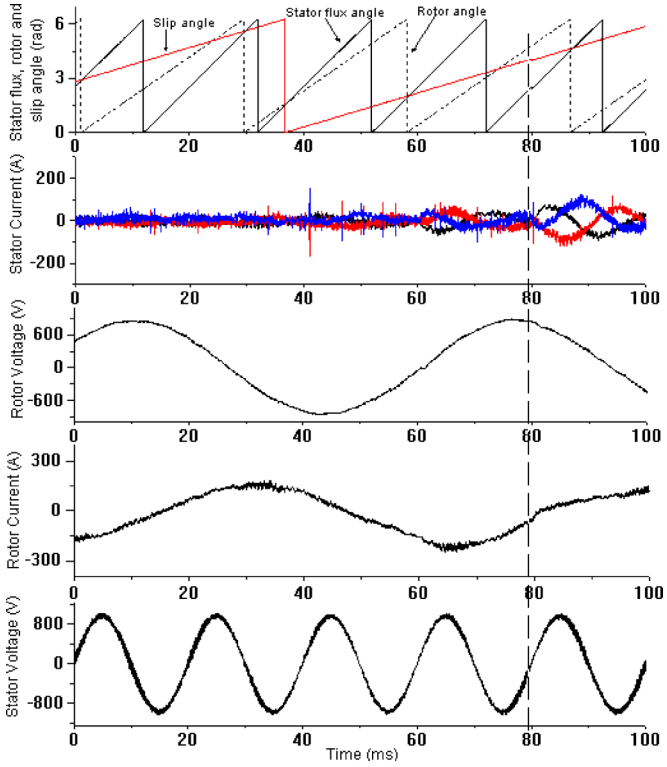

Fig. 13. Experiment result with power outer loops ($\Delta\theta_{sr} \approx 0.1$, the external disturbance comes at the rising edge of the stator voltage).

Fig. 11 is for the case when $\Delta\theta_{sr}$ is 0.628 rad. Fig. 11 show:

1) the stator flux angle, rotor angle, and slip angle;
2) three-phase stator current;
3) the rotor voltage (line AB, pulsewidth modulation (PWM) switching is removed by a 500-Hz low-pass filter);
4) the rotor current (phase A); and
5) the stator voltage (line AB).

The rotor current and voltage become distorted. The stator currents are larger than the situation when the angle is correct. The shapes of the waveforms are similar to those shown in Fig. 5, which has been obtained by simulation.

Fig. 12 shows the case when $\Delta\theta_{sr}$ is a larger angle error of 3.14 rad. The rotor current and voltage become distorted. The stator currents are larger than that shown in Fig. 11. The shapes of the waveforms are similar to those shown in Fig. 6, which has been obtained by simulation studies. But no matter how much the angle deviation is, the system can still kept stable, which has been analyzed in the previous section.

C. Experiment Result With Power Outer Loop

In this section, the control strategy is implemented with the outer power loop. For safety reasons, the stator active power and reactive power references were set to zero. During the tests, the rotor speed was 0.7 of the synchronous speed. Two tests were performed and the waveforms are shown in Figs. 13 and 14.

Fig. 13 is for the case when $\Delta\theta_{sr}$ is small. The small error arises from the presence of pickup noise close to the upward zero-crossing stator voltage illustrated in Fig. 3(c). Fig. 13 show:

1) the stator flux angle, rotor angle, and slip angle;
2) the three-phase stator current;

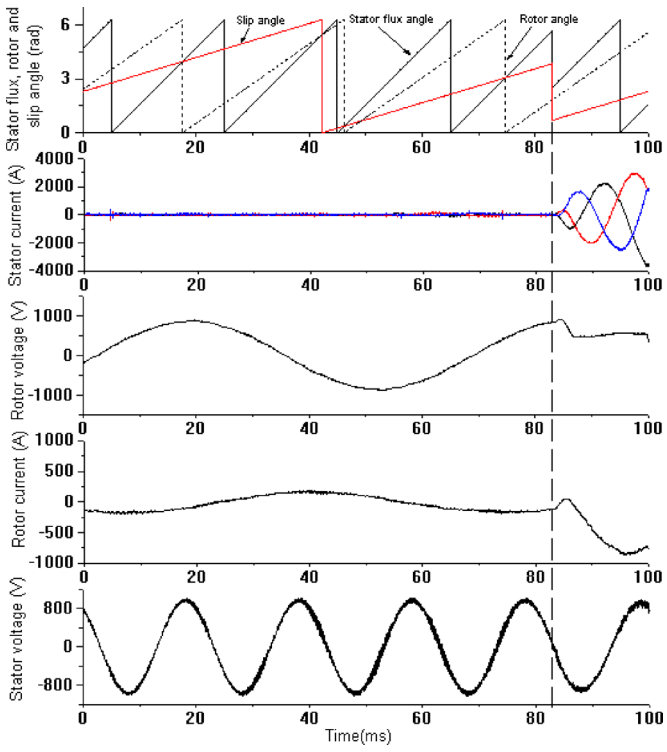

Fig. 14. Experiment result with power outer loops ($\Delta\theta_{sr} = 3.14$, the external disturbance comes at the falling edge of the stator voltage).

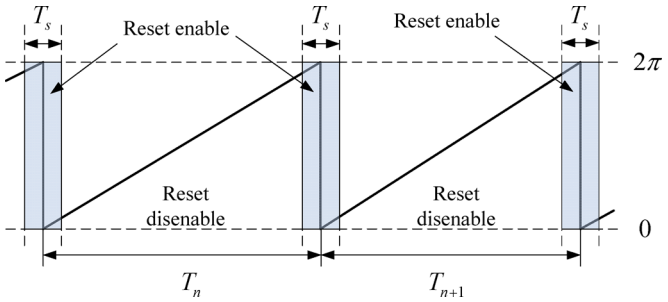

Fig. 15. Method to protect against erroneous pickup: enable and disenable zones to reset position counter.

3) the rotor voltage (line AB, PWM switching is removed by a 500-Hz low-pass filter);
4) the rotor current (phase A); and
5) the stator voltage (line AB).

The rotor current becomes distorted and the stator currents are very much larger than those for zero active power and reactive power references. The shapes of the waveforms are similar to those shown in Fig. 8, which has been obtained by simulation.

Fig. 14 shows the case when $\Delta\theta_{sr}$ is large. This occurs when the external disturbances are close to the falling edge of the stator voltage, as shown in Fig. 3 ($\Delta\theta_{sr} \cong 180^\circ$). The stator currents increase exponentially, indicating unstable negative damping. The shapes of the waveforms are similar to those shown in Fig. 9, which has been obtained by simulation studies.

The value of stator current reaches 3000 A, which is three times of the rated current. It has been possible to measure such large currents because the safety protection limit has been raised. This is very dangerous. One IGBT of the rotor-side converter has exploded in the experiment.

VII. Method to Protect System From External Disturbance

A. Incremental Position Encoder

From Fig. 2, one is reminded that Z pulse of the incremental position encoder resets the counter whose reading represents the rotor electrical angle. Normally, the Z pulse appears at 360 mechanical degrees. The angular error $\Delta\theta_{sr}$ comes from noise pickup, which is mistaken for a Z pulse. The adopted method of protection against such pickups, as illustrated in Fig. 15, consists of disenabling the counter reset, except for the narrow time window of width T_s when the Z pulse is expected. But the arrival of the Z pulse depends on the rotor speed. Although the time period T_{n+1} in the current (n+1)th cycle remains unknown, it can be estimated as being not very different from T_n of the preceding *n*th cycle. This is because the moment of inertia of the turbine–rotor system is large (*H* can be as large as 4 s). By storing T_n in memory and allowing for a tolerance window T_s, the Z pulse is accepted when

$$\left[\left(T_n - \frac{T_s}{2}\right) \le t \le \left(T_n + \frac{T_s}{2}\right)\right] \tag{35}$$

and the reset of the counter is enabled.

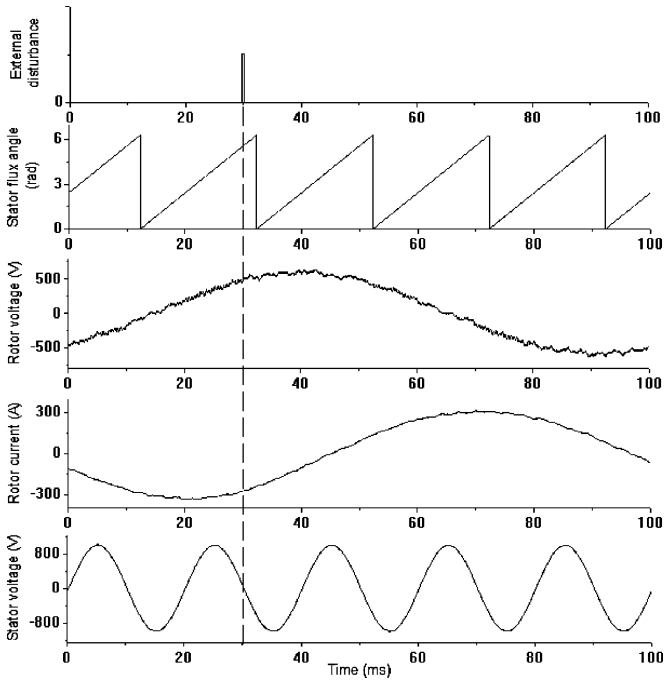

Fig. 16. Experiment result when the proposed method is used.

The maximum angle deviation can be calculated as

$$\Delta\theta_{sr} = \pi\frac{T_s}{T_n}. \tag{36}$$

B. Hardware PLL

From Fig. 3, one can observed that the hardware PLL also contributes to $\Delta\theta_{sr}$ when the pickup noise is mistaken for a reset command. The solution of Fig. 15 is also adopted. The ac supply frequency is closely regulated by the utility, so that T_n is a very good estimate in the enabling window of (35) for the (n+1)th cycle.

C. Test of Protection System

Over an 8-h period, recording monitors show that the noise continue to be picked at about the same rate as in the earlier 4-h period. However, unscheduled pulses in the Z channel are ignored because the counter is disenabled. The same applies for protected hardware PLL.

Fig. 16 shows the external disturbances comes at the falling edge of the stator voltage in the experiment. The waveforms are:

1) the position of external disturbance;
2) the stator flux angle;
3) the rotor voltage (line AB, PWM switching is removed by a 500-Hz low-pass filter);
4) the rotor current (phase A); and
5) the stator voltage (line AB).

With the aforementioned protection method, this disturbance was ignored and the system operation was not affected.

VIII. Conclusion

The paper has shown that occasional exploded IGBTs in the controls of vector-controlled DFIGs can be due to erroneous measurements from hardware PLL and incremental position encoders. This conclusion has been reached by analysis, which has been verified by digital simulations and experimental tests. Destructively large currents in the DFIG can be due to: 1) the erroneous measurements causing the DFIG to perceive very large *P–Q* reference settings or 2) the system consisting of the DFIG under vector control becoming unstable. The experimental results were taken from a 1.5-MW DFIG intended for a wind turbine. The paper has a simple protection scheme, which has been found to be promising in a short trial period.

Appendix

A. Machine Parameters

Parameters of the 1500-kW DFIG in Simulation and Experiment

Rated power	1560kW
Stator voltage	690V
Stator resistance	0.0023 Ω
Rotor resistance	0.002 Ω
Stator leakage reactance	0.0159 Ω
Rotor leakage reactance	0.0271 Ω
Mutual reactance	1.22 Ω
Leakage factor	0.0343
Stator/rotor turns ratio	0.33
Number of pole pairs	2

B. Controller's Parameters

$$k_p^c = 2.5,\ k_i^c = 1,\ k_p^p = 0.7, \text{ and } k_i^p = 0.3.$$

Acknowledgment

The authors gratefully acknowledge the contributions of Dr. Li, Z. Li, and X. Huang for their help on the experiment.

References

[1] L. Shi, Z. Xu, J. Hao, and Y. Ni, "Modelling analysis of transient stability simulation with high penetration of grid-connected wind farms of DFIG type," *Wind Energy*, vol. 10, no. 4, pp. 303–320, 2007.

[2] R. Pena, J. C. Clare, and G. M. Asher, "Doubly fed induction generator using back-to-back PWM converters and its application to variable-speed wind-energy generation," *Proc. Inst. Electr. Eng., Electr. Power. Appl.*, vol. 143, no. 3, pp. 231–241, 1996.

[3] A. Tapia, G. Tapia, J. X. Ostolaza, and J. R. Saenz, "Modeling and control of a wind turbine driven doubly fed induction generator," *IEEE Trans. Energy Convers.*, vol. 18, no. 2, pp. 194–204, Jun. 2003.

[4] S. Muller, M. Deicke, and R. W. De Doncker, "Doubly fed induction generator systems for wind turbines," *IEEE Ind. Appl. Mag.*, vol. 17, no. 1, pp. 26–33, May/Jun. 2002.

[5] F. M. Hughes, O. Anaya-Lara, N. Jenkins, and G. Strbac, "Control of DFIG-based wind generation for power network support," *IEEE Trans. Power Syst.*, vol. 20, no. 4, pp. 1958–1966, Nov. 2005.

[6] S. Baike and O. Boon-Teck, "Novel sensorless decoupled P-Q control of doubly-fed induction generator (DFIG) based on phase locking to gamma-delta frame," in *Proc. Power Electron. Spec. Conf., 2005 (PESC 2005) IEEE 36th*, pp. 2670–2675.

[7] B. Shen, B Mwinyiwiwa, Y. Zhang, and B.-T. Ooi, "Sensorless maximum power point tracking of wind by DFIG using rotor position phase lock loop (PLL)," *IEEE Trans. Power Electron.*, vol. 24, pp. 942–951, Apr. 2009.

[8] P. Kundur, *Power System Stability and Control*, 1st ed. New York: McGraw-Hill, 1994.

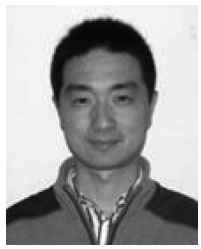

Zhong Wang (S'09) received the B.S. and M.S. degrees in electrical engineering from Huazhong University of Science and Technology, Wuhan, China, in 2003 and 2006, respectively. Currently, he is working toward the Ph.D. degree in the Department of Electrical Engineering, Tsinghua University, Beijing, China.

His current research interests include wind power generator modeling and control.

Guo-Jie Li received the B.S. and M.S. degrees in electrical engineering from Tsinghua University, Beijing, China, in 1989 and 1993, respectively, and the Ph.D. degree from the School of Electrical and Electronic Engineering, Nanyang Technological University, Singapore, in 1999.

Currently, he is an Associate Professor in the Department of Electrical Engineering, Tsinghua University, where he is the Head of the Dynamic Simulation Power System Laboratory. His current research interests include power system analysis and control, wind power analysis and control, voltage source converter high-voltage dc, and power quality.

Yuanzhang Sun (M'99–SM'01) received the B.S. degree from Wuhan University of Hydro and Electrical Engineering, Wuhan, China, in 1978, the M.S. degree from the Electric Power Research Institute (EPRI), Beijing, China, in 1982, and the Ph.D. degree from Tsinghua University, Beijing, in 1988, all in electrical engineering.

From 1982 to 1985, he was with the Power System Research Department, EPRI. Currently, he is a Chair Professor of the Department of Electrical Engineering and the Vice Director of the State Key Lab of Power System Control and Simulation, Tsinghua University. He is also the Dean of the School of Electrical Engineering, Wuhan University, Wuhan. His research interests include power system dynamics and control, voltage stability and control, and reliability.

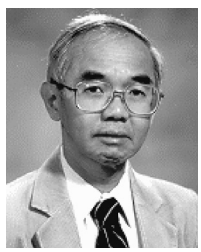

Boon Teck Ooi (S'69–M'71–SM'85–F'03–LF'05) was born in Malaysia. He received the B.Eng. degree (honors) from the University of Adelaide, Adelaide, Australia, the M.S. degree from Massachusetts Institute of Technology, Cambridge, and the Ph.D. degree from McGill University, Montreal, QC, Canada.

He is currently a Professor in the Department of Electrical and Computer Engineering, McGill University.